

Mass and energy balance calculations for artificial ice reservoirs (Icestupas)

Suryanarayanan Balasubramanian^{1*}, Martin Hoelzle¹, Michael Lehning²,
Sonam Wangchuk³, Johannes Oerlemans⁴, Felix Keller^{5,6} and Jordi Bolíbar⁴

¹ University of Fribourg, Fribourg, Switzerland

² WSL Institute for Snow and Avalanche Research, Davos, Switzerland

³ Himalayan Institute of Alternatives Ladakh, Leh, India

⁴ Institute for Marine and Atmospheric Research, Utrecht University, Utrecht, The Netherlands

⁵ Academia Engiadina, Samedan, Switzerland

⁶ ETH, Zürich, Switzerland

Correspondence*:

Suryanarayanan Balasubramanian

suryanarayanan.balasubramanian@unifr.ch

2 ABSTRACT

Artificial Ice Reservoirs (AIRs) can successfully store water during winter and release the water during spring and summer. This makes them a reliable fresh water resource for irrigation in dry environments. Several AIRs have been built but studies of their water storage capacity and efficiency are scarce. This study models a cone-shaped AIR popularly called Icestupa. Processes involved in the development and temporal evolution of an Icestupa are calculated by a physically-based model using equations governing the heat transfer, vapour diffusion and transport of water that undergoes phase changes. These processes were quantified using meteorological data in conjunction with fountain spray information (mass input of an AIR) to estimate the quantity of frozen, melted, evaporated and runoff water for three sites in Switzerland and one in India. At these measurement sites, AIR were built for model validation purposes. The model was further tested by performing a sensitivity and uncertainty study showing that the most sensitive parameters are the ice emissivity and the temperature threshold used to determine precipitation phase. Model calculations estimate that the AIR stored about % of the total water sprayed as ice.

Keywords: iceshelf, mass balance, water storage, climate change adaptation, geoengineering

1 INTRODUCTION

Seasonal snow cover, glaciers and permafrost are expected to change their water storage capacity due to climate change with major consequences for downriver water supply (Immerzeel et al., 2019). The challenges brought about by these changes are especially important for dry mountain environments such as in Central Asia or the Andes, which directly rely on the seasonal meltwater for their farming and drinking needs (Hoelzle et al., 2019; Apel et al., 2018; Buytaert et al., 2017; Chen et al., 2016; Unger-Shayesteh et al., 2013). Some villages in Ladakh, India have already been forced to relocate due to glacial retreat and the corresponding loss of their main fresh water resources (Grossman, 2015).



Figure 1. Icestupa in Ladakh, India on March 2017 was 24 m tall and contained around 3700 m³ of water.
Picture Credits: Lobzang Dadul

24 Artificial ice reservoirs (AIRs) have been considered to be a feasible way to adapt to these changes (Hock
25 et al., 2019; Nüsser et al., 2019b). An AIR is a human-made ice structure typically constructed during the
26 cold winter months and designed to slowly release freshwater during the warm and dry spring and summer
27 months. The main purpose of AIRs is irrigation. Therefore, AIRs are designed to store water in the form of
28 ice as long into the summer as possible. The energy required to construct an AIR is usually derived from
29 the gravitational head of the source water body. Some are constructed horizontally by freezing water using
30 a series of checkdams and others are built vertically by spraying water through fountain systems (Nüsser
31 et al., 2019a). The latter are colloquially referred to as Icestupas and are the subject of this study.

32 A typical Icestupa just requires a pipeline attached to a vertically mounted metal pipe with a fountain
33 nozzle for construction. Their water source is usually a high altitude lake or glacial stream. Due to the
34 altitude difference between the pipeline input and fountain output, water ejects from the fountain nozzle as
35 droplets that eventually lose their latent heat to the atmosphere and accumulate as ice around the metal pipe.
36 The fountain nozzle is raised through addition of further pipes as and when significant ice accumulates.
37 Typically, a dome of branches is constructed around the metal pipe so that such pipe extensions can be
38 done from within this dome. During the winter, the fountain is manually activated from sunset to sunrise.
39 Threads, tree branches and fishing nets are used to guide and accelerate the ice formation.

40 Since their invention in 2013 (Wangchuk, 2014), Icestupas have gained widespread publicity in the region
41 of Ladakh, Northern India since they require very little infrastructure, skills and energy to be constructed
42 in comparison to other water storage technologies. Compared to other AIR geometries, Icestupas (Fig.
43 1) can be built at lower altitudes and last much longer into the summer than other types of ice structures
44 (Wangchuk, 2014). However, to date, no reliable estimates exist about the amount of sprayed water that
45 is necessary to create them and the meltwater they provide (Nüsser et al., 2019a). Rough estimates of
46 Icestupa meltwater in Ladakh suggest that the water loss during the construction process is considerable
47 (see Appendix 8.1). A complete set of measurements of the water storage and energy balance are required
48 to understand the cause of the water losses better and increase the construction efficiency.

49 In this paper, we aim to develop a physically-based model of a vertical AIR (or Icestupa) that can quantify
50 their storage efficiency using existing weather and water usage information. Mass and energy balance



Figure 2. Bird's eye view of the CH21 AIR

51 equations were used to estimate the quantity of water frozen, melted, evaporated and runoff. Sensitivity
 52 and uncertainty analysis were performed to identify the most critical parameters and the variance caused
 53 by them. For validation, we chose four AIR built across the winters of 2019, 2020 and 2021 in India and
 54 Switzerland. Our model and validation experiments provide first steps towards evaluating the effectiveness
 55 of a vertical AIR for irrigation and allow us to outline some preliminary guidelines for consideration when
 56 a construction of an Icestupa for water storage is envisaged.

2 STUDY SITES

57 To accurately calibrate, estimate and validate the ice volume of AIR the model requires three kinds of
 58 measurements namely, weather, water and ice volume. So through the winters of 2019, 2020 and 2021
 59 several scientific AIR were constructed by teams in Switzerland and India. Here we present the results of
 60 three scientific AIR which have a relatively complete dataset associated with them as shown in Table 1.

61 2.1 Measurement sites

62 The Guttannen (CH21) site in the Bern region lies at 1047 m a.s.l.. In the winter (Oct-Apr), mean daily
 63 minimum and maximum air temperatures vary between -13 and 15 °C. Clear skies are rare, averaging
 64 around 7 days during winter (Meteoblue, 2020). The site was situated adjacent to a stream resulting in high
 65 humidity values across the study period as shown in Fig. 2. The fountain used for spraying water had an
 66 initial height of 2.3 m. The water was transferred from a spring water source and flowed via a flowmeter to
 67 the nozzle. In addition, a webcam guaranteed a continuous survey of the site during the construction of the
 68 AIR.

69 The CH21 AIR was constructed by Guttannen Bewegt Association on a garden adjacent to a stream in
 70 Guttannen, Switzerland. To initiate the ice formation process, tree branches were laid covering the fountain
 71 pipe. The fountain height varied between 2 to 5 m during the construction period. Fountain operation was
 72 guided by temperature conditions.

73 The Gangles(IN21) site in the Ladakh region lies at 4025 m a.s.l..

74 2.2 Weather measurements

75 Air temperature, relative humidity, wind speed, pressure, longwave, shortwave direct and diffuse radiation
76 are required to calculate the surface energy balance of an AIR.

77 For the CH site, the primary weather data source was a meteoswiss AWS located 184 m away. In addition,
78 we used ERA5 reanalysis dataset (Copernicus Climate Change Service (C3S), 2017) for filling data gaps
79 and adding data that were not measured directly as shown in Fig. 3. Zero wind speed values were recorded
80 whenever snow accumulated on the ultrasonic wind sensor. It was assumed this was the cause when null
81 wind speeds were observed continuously for atleast 3 hours. All such null values were replaced using the
82 ERA5 dataset.

83 The ERA5 reanalysis dataset has a good correlation with lower elevation sites in Switzerland (Scherrer,
84 2020). The ERA5 grid point chosen (Latitude 46° 38' 24" N, Longitude 8° 15' 00" E) for the CH21 site was
85 around 3.6 km away from the actual site. All the ERA5 variables were therefore fitted with the meteoswiss
86 dataset via linear regressions.

87 For the IN site, the primary weather data source was a campbell weather station located adjacent to the
88 AIR. In addition, we used another campbell AWS located 12 km away for filling data gaps and adding data
89 that were not measured directly as shown in Fig. 3.

90 2.3 Discharge measurements

91 The water flow rate or discharge was measured via an ultrasonic sensor attached to the fountain supply
92 pipeline. However, due to various malfunctions, the discharge measurements were very sparse and could
93 not be extrapolated for the complete measurement period for both the CH and In site. Instead the discharge
94 duration was first determined and then the available discharge measurement was used to determine the
95 average discharge quantity d_{mean} during these periods.

96 For the CH site, the fountain was never switched off so the discharge duration was extrapolated from
97 just from one fountain on and off event each. The discharge quantity during this duration varied as shown
98 by the sparse flowmeter measurements captured. Here we assume a constant discharge quantity d_{mean}
99 calculated from the mean of the available flowmeter measurements.

100 For the IN site, even though the fountain was never manually switched off, there were many pipeline
101 freezing events that interrupted the discharge duration. So discharge rate was extrapolated to be the mean
102 discharge d_{mean} except during these pipeline freezing events.

103 2.4 Ice volume measurements

104 Several Drone flights were conducted in the CH and IN sites. The DEM generated through these flights
105 were analysed to obtain the circumference and volume of the ice structure. The mean circumference
106 measured during the fountain duration was set as the spray radius (r_{spray}) and the first drone flight was used
107 to set the dome volume (V_{dome}) for model initialisation. The ice volume data was later used for calibration
108 and validation of the model.

3 MODEL SETUP

109 A bulk energy and mass balance model is used to calculate the amounts of ice, meltwater, water vapour
110 and runoff water of the AIR every hour. This model consists of four modules which estimates the AIR, a)
111 geometric evolution , b) energy balance, c) surface temperature and d) mass balance.

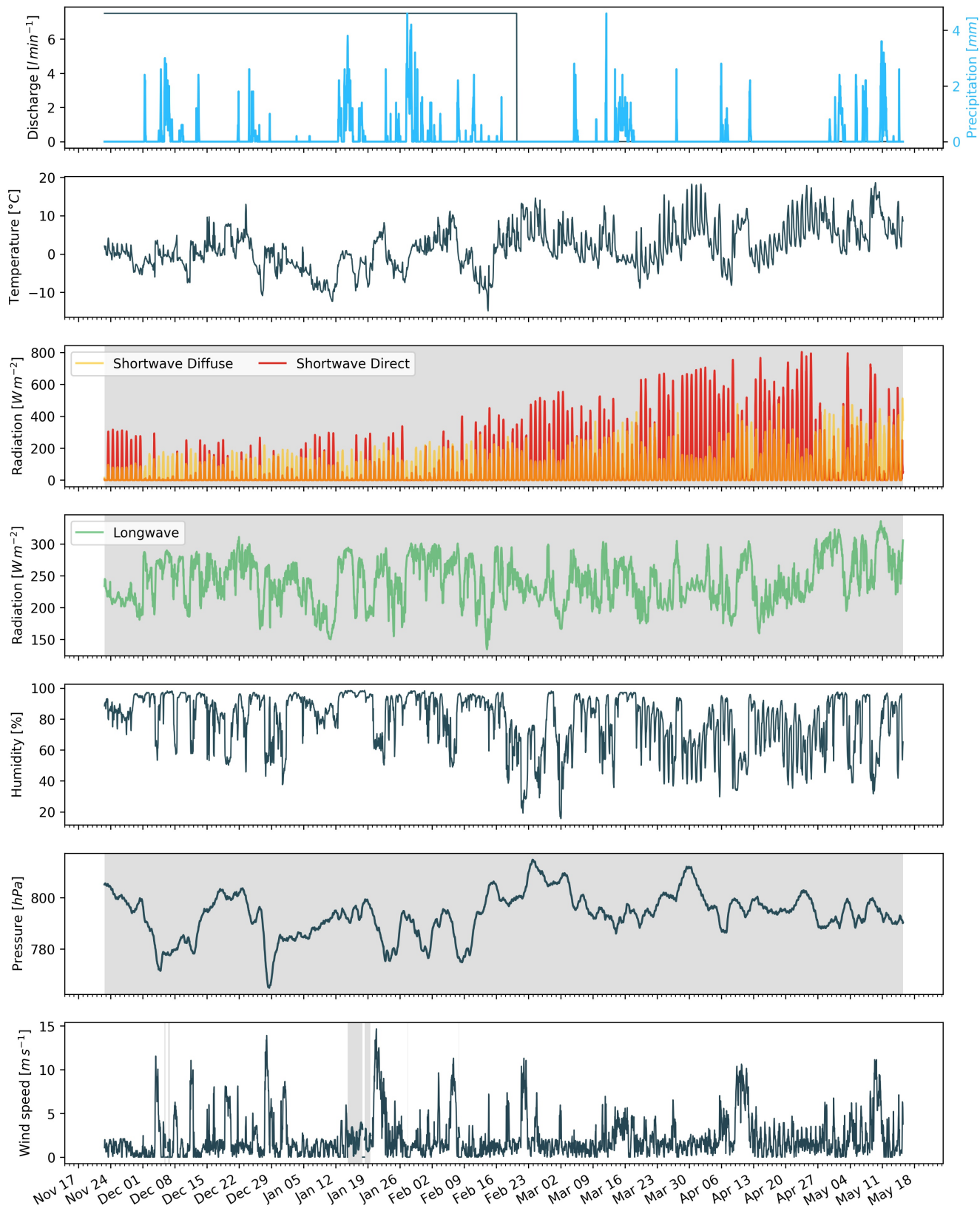
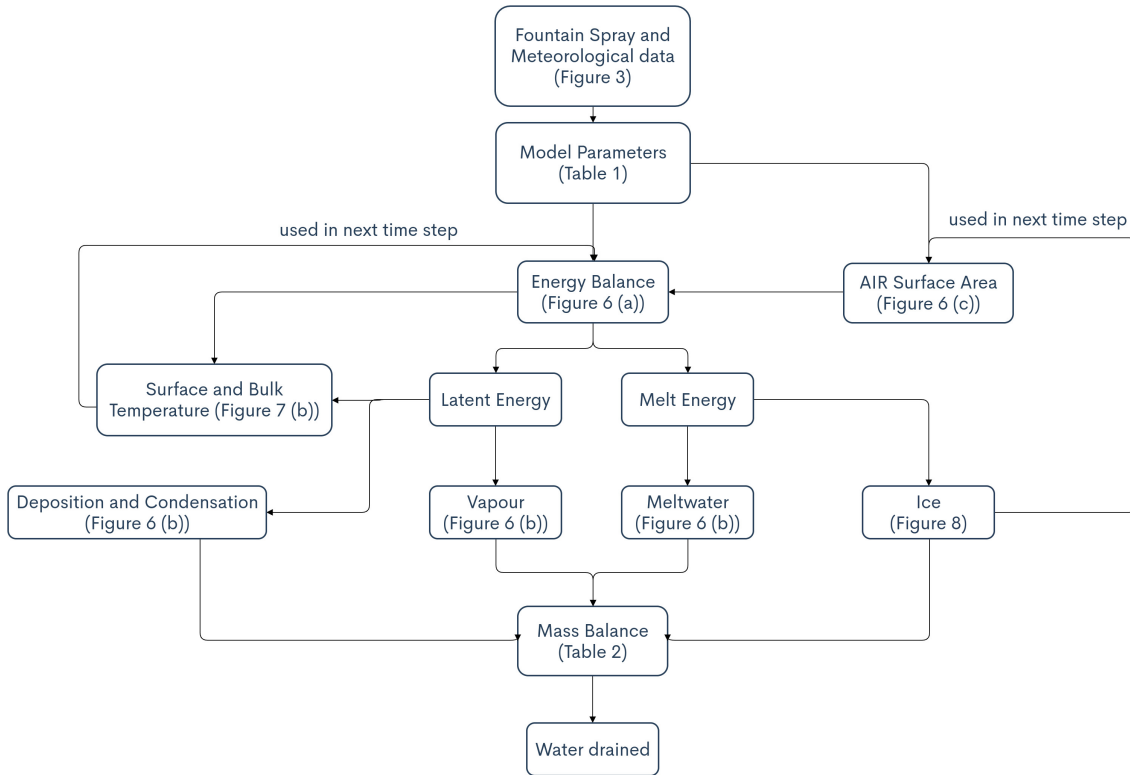


Figure 3. Measurements at the AWS of CH21 were used as main model input data in hourly frequency. Missing data, data gaps and errors were filled from the ERA5 dataset (shaded regions).

Table 1. The Scientific AIR

AIR	Gangles, 2021	Guttannen, 2021	Guttannen, 2020
Shortname	IN21	CH21	CH20
Altitude [m a.s.l.]	4025	1047	1047
Fountain Duration	Jan 18 - Mar 10	Nov 22 - Feb 20	Jan 3 - Mar 8
Drone Flights	6	9	3
r_{spray} [m]	10.8	6.9	7.7
V_{dome} [m^3]	78.5	13.2	23.9
d_{mean} [l/min]	60	7.5	7.5

**Figure 4.** Model schematic showing the algorithm used in the model at every time step. Further details about the variables can be found in the associated tables and figures.

112 3.1 Geometric evolution

113 Radius r_{ice}^i and height h_{ice}^i define the dimensions of the AIR assuming its geometry to be a cone. The
114 surface area A^i exposed to the atmosphere and volume V^i are:

$$A = \pi \cdot r_{ice} \cdot \sqrt{r_{ice}^2 + h_{ice}^2} \quad (1)$$

$$V = \frac{\pi}{3} \cdot r_{ice}^2 \cdot h_{ice} \quad (2)$$

115 Note that we do not specify the time step superscript i of the shape variables A , V , r_{ice} and h_{ice} for
 116 brevity. The equations used henceforth display model time step superscript i only if it is different from the
 117 current time step.

118 With the mass of the AIR M_{ice} , its current volume can also be expressed as:

$$V = M_{ice} / \rho_{ice} \quad (3)$$

119 where ρ_{ice} is the density of ice (917 kg m^{-3}).

120 The influence of the AIR fountain is parameterised by the fountain water temperature T_w and its spray
 121 radius r_{spray} . The initial radius r_0 of the AIR is assumed to be r_{spray} . The initial height h_0 depends on the
 122 dome volume V_{dome} used to construct the AIR as follows:

$$h_0 = \Delta x + \frac{3 \cdot V_{dome}}{\pi r_{spray}^2} \quad (4)$$

123 where Δx is the surface layer thickness (defined in Section 3.2)

124 During subsequent time steps, the dimensions of the AIR evolve assuming a uniform ice formation and
 125 decay across its surface area with an invariant slope $s_{cone} = \frac{h_{ice}}{r_{ice}}$. During these time steps, the volume is
 126 parameterised using Eqn. 2 as:

$$V = \frac{\pi \cdot r_{ice}^3 \cdot s_{cone}}{3} \quad (5)$$

127 However, the Icestupa cannot outgrow the maximum range of the water droplets ($(r_{ice})_{max} = r_F$).
 128 Combining equations 2, 4, 3 and 5, the geometric evolution of the Icestupa at each time step i can be
 129 determined by considering the following rules:

$$(r_{ice}, h_{ice}) = \begin{cases} (r_{spray}, h_0) & \text{if } i = 0 \\ (r_{ice}^{i-1}, \frac{3 \cdot M_{ice}}{\pi \cdot \rho_{ice} \cdot (r_{ice}^{i-1})^2}) & \text{if } r_{ice}^{i-1} \geq r_F \text{ and } \Delta M_{ice} > 0 \\ (\frac{3 \cdot M_{ice}}{\pi \cdot \rho_{ice} \cdot s_{cone}})^{1/3} \cdot (1, s_{cone}) & \text{otherwise} \end{cases} \quad (6)$$

130 where $\Delta M_{ice} = M_{ice}^{i-1} - M_{ice}^{i-2}$

131 3.2 Energy Balance

132 The energy balance equation (Hock, 2005) for the AIR is formulated as follows:

$$q_{SW} + q_{LW} + q_L + q_S + q_F + q_G = q_{surf} \quad (7)$$

133 where q_{surf} is the surface energy flux in [W m^{-2}]; q_{SW} is the net shortwave radiation; q_{LW} is the net
 134 longwave radiation; q_L and q_S are the turbulent latent and sensible heat fluxes. q_F represents the heat
 135 exchange of the fountain water droplets with the AIR ice surface. q_G represents ground heat flux between
 136 Icestupa surface and Icestupa interior. Energy transferred in the direction of the ice surface is always
 137 denoted as positive and away as negative.

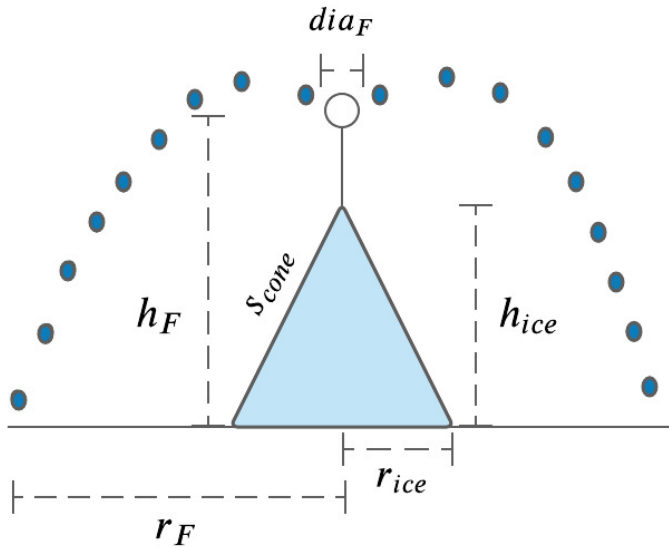


Figure 5. Shape variables and fountain constants of the CH21 Icestupa. r_{ice} is the radius, h_{ice} is the height and s_{cone} is the slope of the ice cone. r_{spray} is the spray radius, h_F is the height and dia_F is the nozzle diameter of the fountain.

138 Equation 7 is usually referred to as the energy budget for “the surface”, but practically it must apply
 139 to a surface layer of ice with a finite thickness Δx . The energy flux acts upon the Icestupa surface layer
 140 which has an upper and a lower boundary defined by the atmosphere and the ice body of the Icestupa,
 141 respectively. The parameter selection for Δx is based on the following two arguments: (a) the ice thickness
 142 Δx should be small enough to represent the surface temperature variations every model time step Δt and
 143 (b) Δx should be large enough for these temperature variations to not reach the bottom of the surface layer.
 144 Therefore, we introduced a 20 mm thick surface layer for a model time step of 1 hour, over which the
 145 energy balance is calculated. A sensitivity analysis was later performed to understand the influence of this
 146 factor. Here, we define the surface temperature T_{ice} to be the modelled average temperature of the Icestupa
 147 surface layer and the energy flux q_{surf} is assumed to act uniformly across the Icestupa area A .

3.2.1 Net Shortwave Radiation q_{SW}

149 The net shortwave radiation q_{SW} is computed as follows:

$$q_{SW} = (1 - \alpha) \cdot (SW_{direct} \cdot f_{cone} + SW_{diffuse}) \quad (8)$$

150 where SW_{direct} and $SW_{diffuse}$ are the ERA5 direct and diffuse short wave radiation, α is the modelled
 151 albedo and f_{cone} is the area fraction of the ice structure exposed to the direct shortwave radiation.

152 We model the albedo using a scheme described in Oerlemans and Knap (1998). The scheme records the
 153 decay of albedo with time after fresh snow is deposited on the surface. δt records the number of time steps
 154 after the last snowfall event. After snowfall, albedo changes over a time step, δt , as

$$\alpha = \alpha_{ice} + (\alpha_{snow} - \alpha_{ice}) \cdot e^{(-\delta t)/\tau} \quad (9)$$

155 where α_{ice} is the bare ice albedo value (0.35), α_{snow} is the snow ice albedo value (0.85) and τ is a decay
 156 rate, which determines how fast the albedo of the ageing snow reaches this value. The decay rate τ is
 157 assumed to have a base value of 10 days similar to values obtained by Schmidt et al. (2017) for wet surfaces
 158 and its maximal value is set based on observations by Oerlemans and Knap (1998) as shown in Table 2.
 159 Furthermore, the albedo α varies depending on the water source that formed the current Icestupa surface.
 160 Correspondingly, the albedo is reset to the value of bare ice albedo if the fountain is spraying water onto
 161 the current ice surface and to the value of fresh snow albedo if a snowfall event occurred. Snowfall events
 162 are assumed if the air temperature is below $T_{ppt} = 1^{\circ}C$ (Fujita and Ageta, 2000).

163 The area fraction f_{cone} of the ice structure exposed to the direct shortwave radiation depends on the
 164 shape considered. The direct solar radiation incident on the AIR surface is first decomposed into horizontal
 165 and vertical components using the solar elevation angle θ_{sun} . For a conical shape, half of the total curved
 166 surface is exposed to the vertical component of the direct shortwave radiation and the projected triangle
 167 of the curved surface is exposed to the horizontal component of the direct shortwave radiation. The solar
 168 elevation angle θ_{sun} used is modelled using the parametrisation proposed by Woolf (1968). Accordingly,
 169 f_{cone} is determined as follows:

$$f_{cone} = \frac{(0.5 \cdot r_{ice} \cdot h_{ice}) \cdot \cos\theta_{sun} + (\pi \cdot r_{ice}^2 / 2) \cdot \sin\theta_{sun}}{\pi \cdot r_{ice} \cdot (r_{ice}^2 + h_{ice}^2)^{1/2}} \quad (10)$$

170 The ERA5 diffuse shortwave radiation is assumed to impact the conical Icestupa surface uniformly.

171 3.2.2 Net Longwave Radiation q_{LW}

172 The net longwave radiation q_{LW} is determined as follows:

$$q_{LW} = LW_{in} - \sigma \cdot \epsilon_{ice} \cdot (T_{ice} + 273.15)^4 \quad (11)$$

173 where T_a represents the measured air temperature, T_{ice} is the modelled surface temperature, both
 174 temperatures are given in $^{\circ}C$, $\sigma = 5.67 \cdot 10^{-8} J m^{-2} s^{-1} K^{-4}$ is the Stefan-Boltzmann constant, LW_{in}
 175 denotes the incoming longwave radiation derived from the ERA5 dataset and ϵ_{ice} is the corresponding
 176 emissivity value for the Icestupa surface (see Table 2).

177 3.2.3 Turbulent sensible q_S and latent q_L heat fluxes

178 The turbulent sensible q_S and latent heat q_L fluxes are computed with the following expressions proposed
 179 by Garratt (1992):

$$q_S = c_a \cdot \rho_a \cdot p_a / p_{0,a} \cdot \frac{\kappa^2 \cdot v_a \cdot (T_a - T_{ice})}{(\ln \frac{h_{AWS}}{z_{ice}})^2} \quad (12)$$

$$q_L = 0.623 \cdot L_s \cdot \rho_a / p_{0,a} \cdot \frac{\kappa^2 \cdot v_a (p_{v,a} - p_{v,ice})}{(\ln \frac{h_{AWS}}{z_{ice}})^2} \quad (13)$$

180 where h_{AWS} is the measurement height above the ground surface of the AWS (in m), v_a is the wind
 181 speed in $[m s^{-1}]$, c_a is the specific heat of air at constant pressure ($1010 J kg^{-1} K^{-1}$), ρ_a is the air density
 182 at standard sea level ($1.29 kg m^{-3}$), $p_{0,a}$ is the air pressure at standard sea level ($1013 hPa$), κ is the

183 von Karman constant (0.4), L_s is the heat of sublimation (2848 kJ kg^{-1}) and z_{ice} (1.7 mm) denotes the
 184 roughness length of ice (momentum and scalar). The vapor pressures over air ($p_{v,a}$) and ice ($p_{v,ice}$) was
 185 obtained using the following formulation given in WMO (2018):

$$\begin{aligned} p_{v,a} &= 6.107 \cdot 10^{(7.5 \cdot T_a / (T_a + 237.3))} \\ p_{v,ice} &= (1.0016 + 3.15 \cdot 10^{-6} \cdot p_a - 0.074 \cdot p_a^{-1}) \cdot (6.112 \cdot e^{(22.46 \cdot T_{ice} / (T_{ice} + 272.62))}) \end{aligned} \quad (14)$$

186 where p_a is the measured air pressure in [hPa].

187 3.2.4 Fountain water heat flux q_F

188 The interaction between the fountain water and the ice surface is taken into account by assuming that
 189 the ice surface temperature remains constant at 0°C during time steps when the fountain is active. This
 190 process can be divided into two simultaneous steps: (a) the water temperature T_{water} is cooled to 0°C
 191 and (b) the ice surface temperature is warmed to 0°C . Thus, the heat flux caused by the fountain water is
 192 calculated as follows:

$$q_F = \begin{cases} 0 & \text{if } \Delta M_F = 0 \\ \frac{\Delta M_F \cdot c_{water} \cdot T_{water}}{\Delta t \cdot A} + \frac{\rho_{ice} \cdot \Delta x \cdot c_{ice} \cdot T_{ice}}{\Delta t} & \text{if } \Delta M_F > 0 \end{cases} \quad (15)$$

193 with c_{ice} as the specific heat of ice.

194 3.2.5 Bulk Icestupa heat flux q_G

195 The bulk Icestupa heat flux q_G corresponds to the ground heat flux in normal soils and is caused by the
 196 temperature gradient between the surface layer (T_{ice}) and the ice body (T_{bulk}). It is expressed by using the
 197 heat conduction equation as follows:

$$q_G = k_{ice} \cdot (T_{bulk} - T_{ice}) / l_{ice} \quad (16)$$

198 where k_{ice} is the thermal conductivity of ice ($2.123 \text{ W m}^{-1} \text{ K}^{-1}$), T_{bulk} is the mean temperature of the
 199 ice body within the Icestupa and l_{ice} is the average distance of any point in the surface to any other point in
 200 the ice body. T_{bulk} is initialised as 0°C and later determined from Eqn. 16 as follows:

$$T_{bulk}^{i+1} = T_{bulk} - (q_G \cdot A \cdot \Delta t) / (M_{ice} \cdot c_{ice}) \quad (17)$$

201 Since AIR's typically have conical shapes with $r_{ice} \gg h_{ice}$, we assume that the center of mass of the ice
 202 body is near the base of the fountain. Thus, the distance of every point in the AIR surface layer from the ice
 203 body's center of mass is between h_{ice} and r_{ice} . So we calculate q_G here assuming $l_{ice} = (r_{ice} + h_{ice})/2$.

204 3.3 Surface temperature

205 The available energy q_{surf} can act on the surface of the AIR to a) change its temperature, b) melt ice or
 206 c) freeze ice. So Eqn. 7 can be rewritten as:

$$q_{surf} = q_{freeze/melt} + q_T \quad (18)$$

207 where q_T , q_{freeze} and q_{melt} represent energy associated with process (a), (b) and (c) respectively.

Table 2. Free parameters in the model categorised as constant and uncertain parameters. Base value (B) and uncertainty (U) were taken from the literature. For assumptions (assum.), the uncertainty was chosen to be relatively large (5 %). For measurements (meas.), the uncertainty due to parallax errors is chosen to be (1 %).

Constant Parameters	Symbol	Value	References
Van Karman constant	κ	0.4	B: Cuffey and Paterson
Stefan Boltzmann constant	σ	$5.67 \cdot 10^{-8} W m^{-2} K^{-4}$	B: Cuffey and Paterson
Air pressure at sea level	$p_{0,a}$	1013 hPa	B: Mölg and Hardy
Density of water	ρ_w	$1000 kg m^{-3}$	B: Cuffey and Paterson
Density of ice	ρ_{ice}	$917 kg m^{-3}$	B: Cuffey and Paterson
Density of air	ρ_a	$1.29 kg m^{-3}$	B: Mölg and Hardy
Specific heat of ice	c_{ice}	$2097 J kg^{-1} ^\circ C^{-1}$	B: Cuffey and Paterson
Specific heat of water	c_w	$4186 J kg^{-1} ^\circ C^{-1}$	B: Cuffey and Paterson
Specific heat of air	c_a	$1010 J kg^{-1} ^\circ C^{-1}$	B: Mölg and Hardy
Thermal conductivity of ice	k_{ice}	$2.123 W m^{-1} K^{-1}$	B: Bonales et al.
Latent Heat of Sublimation	L_s	$2848 kJ kg^{-1}$	B: Cuffey and Paterson
Latent Heat of Fusion	L_f	$334 kJ kg^{-1}$	B: Cuffey and Paterson
Surface Parameters		Range	
Temperature threshold for precipitation	T_{ppt}	$1 ^\circ C$	$\pm 1 ^\circ C$
Thickness threshold for precipitation	H_{ppt}	$1 mm w.e.$	$\pm 1 mm w.e.$
Ice Emissivity	ϵ_{ice}	0.95	[0.949,0.993]
Ice Albedo	α_{ice}	0.35	$\pm 5 \%$
Snow Albedo	α_{snow}	0.85	$\pm 5 \%$
Albedo Decay Rate	τ	10 days	[1, 22] days
Surface layer thickness	Δx	20 mm	$\pm 5 \%$
Fountain Parameters		Range	
Spray Radius	r_{spray}		$\pm 5 \%$
Water temperature	T_{water}	$1 ^\circ C$	[0, 5] $^\circ C$
Mean discharge	d_{mean}		l/min

208 To distribute the surface energy flux into these three components, we categorize the model time steps
 209 as freezing or melting events. Freezing events can only occur if there is fountain water available and the
 210 surface energy flux is negative. But just these two conditions are not sufficient as the latent heat energy
 211 can only contribute to temperature fluctuations. So to prevent latent heat energy from turning a melting
 212 event into a freezing event an additional condition namely $(q_{surf} - q_L) < 0$ is required. Thus, freezing and
 213 melting events are identified as follows:

$$q_{freeze/melt} = \begin{cases} q_{freeze} & \text{if } \Delta M_F > 0 \text{ and } q_{surf} < 0 \text{ and } (q_{surf} - q_L) < 0 \\ q_{melt} & \text{otherwise} \end{cases} \quad (19)$$

214 During a freezing event, the available energy ($q_{surf} - q_L$) can either be sufficient or insufficient to
 215 freeze the fountain water available. If insufficient, the additional energy further cools down the surface
 216 temperature. So the surface energy flux distribution during a freezing event can be represented as:

$$(q_{freeze}, q_T) = \begin{cases} (q_{surf} - q_L, q_L) & \text{if } \Delta M_F \geq -\frac{(q_{surf} - q_L)A \cdot \Delta t}{L_f} \\ \left(\frac{\Delta M_F \cdot L_f}{A \cdot \Delta t}, q_{surf} + \frac{\Delta M_F \cdot L_f}{A \cdot \Delta t}\right) & \text{if } \Delta M_F < -\frac{(q_{surf} - q_L)A \cdot \Delta t}{L_f} \end{cases} \quad (20)$$

217 During a melting event, the surface energy flux (q_{surf}) is first used to change the surface temperature to
 218 T_{temp} calculated as:

$$T_{temp} = \frac{q_{surf} \cdot \Delta t}{\rho_{ice} \cdot c_{ice} \cdot \Delta x} + T_{ice} \quad (21)$$

219 If $T_{temp} > 0^\circ C$, then energy is reallocated from q_T to q_{melt} to maintain surface temperature at melting
 220 point. So the surface energy flux distribution during a melting event can be represented as:

$$(q_{melt}, q_T) = \begin{cases} (0, q_{surf}) & \text{if } T_{temp} < 0 \\ \left(\frac{T_{temp} \cdot \rho_{ice} \cdot c_{ice} \cdot \Delta x}{\Delta t}, q_{surf} - \frac{T_{temp} \cdot \rho_{ice} \cdot c_{ice} \cdot \Delta x}{\Delta t}\right) & \text{if } T_{temp} > 0 \end{cases} \quad (22)$$

221 3.4 Mass Balance

222 The mass balance equation for an AIR is represented as:

$$\frac{\Delta M_F + \Delta M_{ppt} + \Delta M_{dep}}{\Delta t} = \frac{\Delta M_{ice} + \Delta M_{water} + \Delta M_{sub} + \Delta M_{runoff}}{\Delta t} \quad (23)$$

223 where M_F is the discharge of the fountain; M_{ppt} is the cumulative precipitation; M_{dep} is the cumulative
 224 accumulation through water vapour deposition; M_{ice} is the cumulative mass of ice; M_{water} is the cumulative
 225 mass of melt water; M_{sub} represents the cumulative water vapor loss by sublimation and M_{runoff} represents
 226 the fountain discharge runoff that did not interact with the AIR. The LHS of equation 23 represents the rate
 227 of mass input and the RHS represents the rate of mass output for an AIR.

228 Precipitation input is calculated as shown in equation 24a where ρ_w is the density of water (1000
 229 $kg m^{-3}$), ppt is the measured precipitation rate in [$m s^{-1}$] and T_{ppt} is the temperature threshold below
 230 which precipitation falls as snow. Here, snowfall events were identified using T_{ppt} as $1^\circ C$. Snow mass
 231 input is calculated by assuming a uniform deposition over the entire circular footprint of the Icestupa.

232 The latent heat flux is used to estimate either the evaporation and condensation processes or sublimation
 233 and deposition processes as shown in equation 24b. During time steps at which surface temperature is
 234 below $0^\circ C$ only sublimation and deposition can occur, but if the surface temperature reaches $0^\circ C$,
 235 evaporation and condensation can also occur. As the differentiation between evaporation and sublimation
 236 (and condensation and deposition) when the air temperature reaches $0^\circ C$ is challenging, we assume
 237 that negative (positive) latent heat fluxes correspond only to sublimation (deposition), i.e. no evaporation
 238 (condensation) is calculated.

239 Since we have categorized every time step as a freezing and melting event, we can determine the meltwater
 240 and ice generated using the associated energy fluxes as shown in equations 24c and 24d. Having calculated

241 all the other mass components the fountain wastewater generated every time step can be calculated using
 242 equation 24e.

$$\frac{\Delta M_{ppt}}{\Delta t} = \begin{cases} \pi \cdot r_{ice}^2 \cdot \rho_w \cdot ppt & \text{if } T_a < T_{ppt} \\ 0 & \text{if } T_a \geq T_{ppt} \end{cases} \quad (24a)$$

$$\left(\frac{\Delta M_{dep}}{\Delta t}, \frac{\Delta M_{sub}}{\Delta t} \right) = \begin{cases} \frac{q_L \cdot A}{L_s} \cdot (1, 0) & \text{if } q_L \geq 0 \\ \frac{q_L \cdot A}{L_s} \cdot (0, -1) & \text{if } q_L < 0 \end{cases} \quad (24b)$$

$$\frac{\Delta M_{water}}{\Delta t} = \frac{q_{melt} \cdot A}{L_f} \quad (24c)$$

$$\frac{\Delta M_{ice}}{\Delta t} = \frac{q_{freeze} \cdot A}{L_f} + \frac{\Delta M_{ppt}}{\Delta t} + \frac{\Delta M_{dep}}{\Delta t} - \frac{\Delta M_{sub}}{\Delta t} - \frac{\Delta M_{melt}}{\Delta t} \quad (24d)$$

$$\frac{\Delta M_{runoff}}{\Delta t} = \frac{\Delta M_F - \Delta M_{ice}}{\Delta t} \quad (24e)$$

243 To estimate the mass of any component at time step i , one can now sum the mass flux estimated above:

$$M_{comp}^i = \sum_{t=0}^{t=i} \left(\frac{\Delta M_{comp}}{\Delta t} \right)_t + M_{comp}^0 \quad (25)$$

244 where

$$M_{comp}^0 = \begin{cases} -V_{dome} * \rho_{ice} & \text{if } M_{comp} = M_{ice} \text{ or } M_F \\ 0 & \text{otherwise} \end{cases} \quad (26)$$

245 Considering AIRs as water reservoirs, we can quantify their potential through the amount of water they
 246 store (storage quantity) and the length of time they store it (storage duration). Another means of comparing
 247 different Icestupas is through their water storage efficiency defined accordingly as:

$$\text{Storage Efficiency} = \frac{M_{water}}{(M_F + M_{ppt} + M_{dep})} \cdot 100 \quad (27)$$

4 MODEL RESULTS

248 The model was forced with meteorological data from 22nd November to 10th May 2021 (Fig. 3) and
 249 various parameters (see Table 2) to calculate the mass and energy balance of the CH21 AIR.

4.1 Energy and mass balance calculation

250 Daily averages of some components of the energy balance are shown in Fig. 6 (b). On average during
 251 the experiment duration, the total energy balance was almost zero. Net shortwave radiation (35 W m^{-2}),
 252 sensible (41 W m^{-2}) and latent heat flux (2 W m^{-2}) with a mostly positive flux towards the surface of the
 253 icestupa were compensated by the net longwave radiation (-47 W m^{-2}), the fountain water heat flux (-13 W m^{-2}) and the freeze/melt energy (-19 W m^{-2}). The contributions of other fluxes were negligible in
 254 comparison.
 255

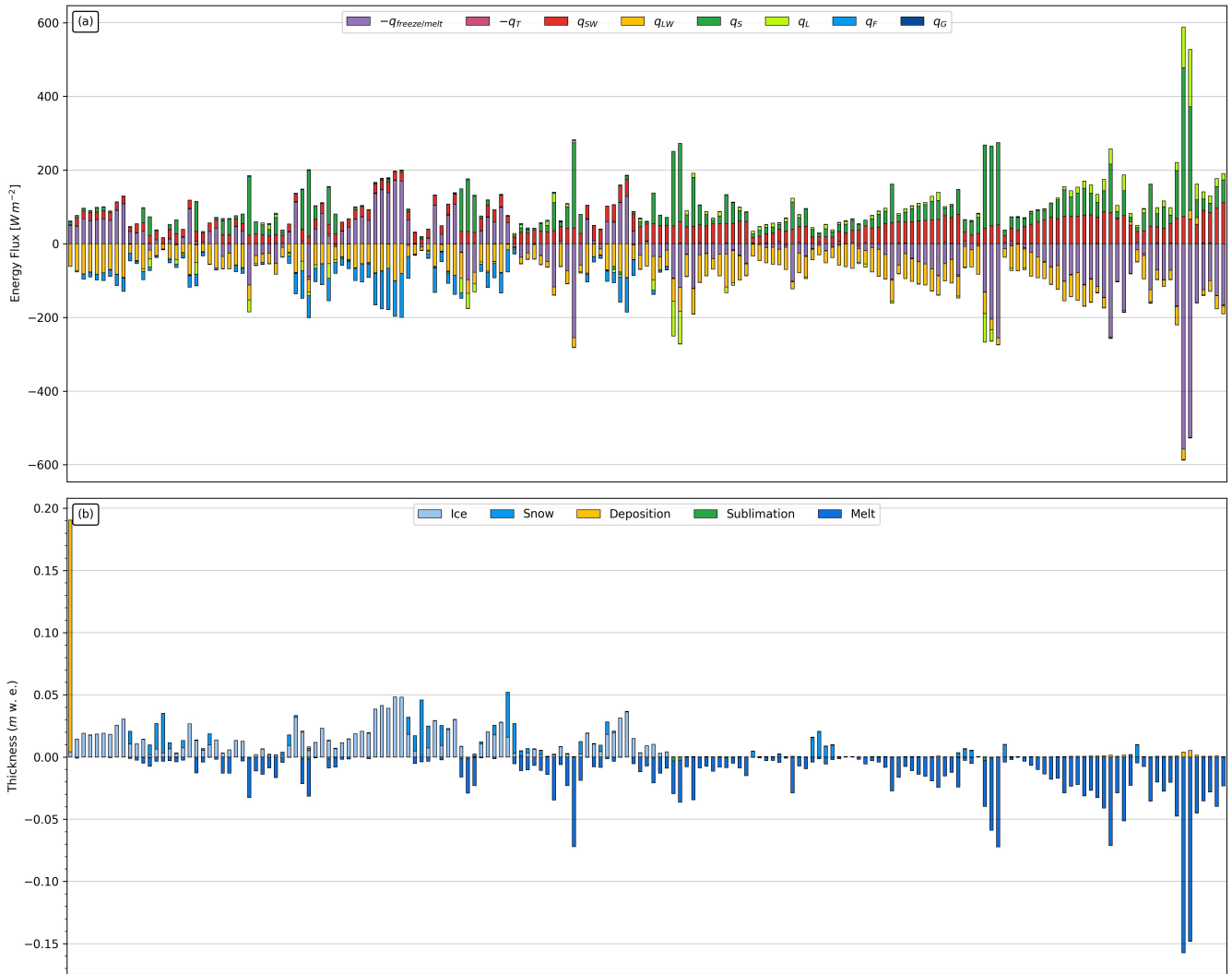


Figure 6. (a) Energy and (b) mass flux components of the CH21 AIR in daily time steps. q_{SW} is the net shortwave radiation; q_{LW} is the net longwave radiation; q_L and q_S are the turbulent latent and sensible heat fluxes. q_F represents the interactions of the fountain water with the AIR surface layer. q_G quantifies the heat conduction process between the AIR surface layer and the ice body.

257 Net shortwave radiation is the main input to, and the most varying energy flux on the ice surface. Its
 258 variability is controlled by the surface albedo α and the area fraction f_{cone} which therefore represent key
 259 variables in the energy balance (Fig. ?? (b)). Although global radiation flux reached a daily maximum
 260 value of 340 W m^{-2} , q_{SW} only went up to 114 W m^{-2} . This is caused by the fact that less than 40 % of
 261 the direct solar radiation influenced the Icestupa surface as shown by the area fraction f_{cone} in Fig. ?? (a).
 262 Snowfall is the atmospheric variable connected most closely and proportionally to albedo. Higher and/or
 263 more frequent snowfall thus decreases the energy available for melt due to the corresponding increase in α .

264 q_{LW} was predominantly negative indicating that this energy balance component drove the freezing of
 265 the ice structure. Daily values of q_{LW} ranged from -101 to 19 W m^{-2} . Turbulent sensible heat flux q_S
 266 contributed mostly to the melt of the ice structure. Daily values of q_S ranged from -3 to 410 W m^{-2} . Daily
 267 values of the turbulent latent heat flux q_L ranged from -90 to 157 W m^{-2} . Since the mean of q_L was positive,
 268 the Icestupa gained mass cumulatively from the atmosphere due to the deposition process. Daily values

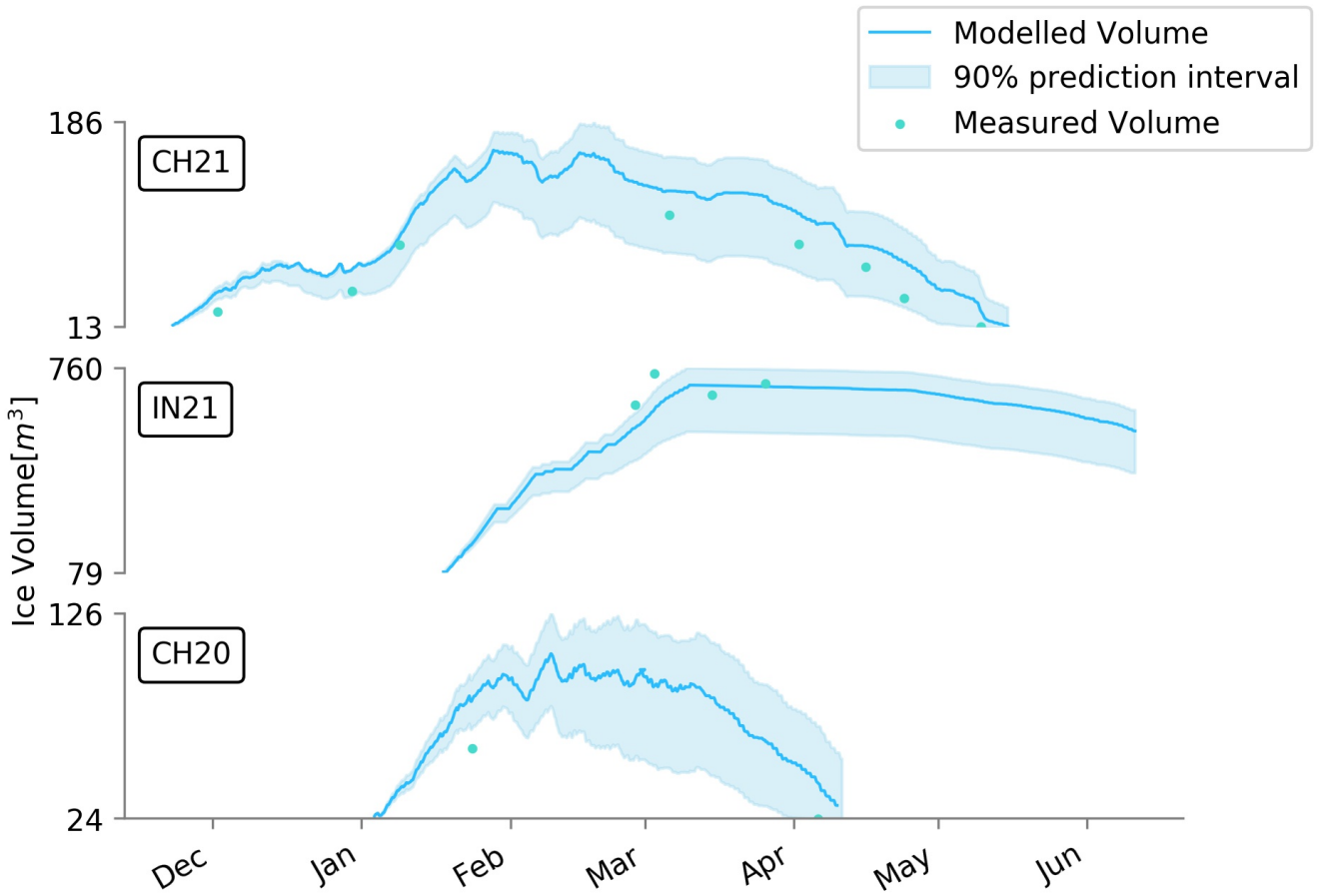


Figure 7. Modelled ice volume during the lifetime of the AIR (blue curve). Green points indicate the validation measurements. The prediction interval is based on the ice volume uncertainty caused by the most sensitive parameters.

of fountain water heat flux ranged from -119 to 4 W m⁻². q_F was also a significant contributor to the freezing process like q_{LW} . So the influence of the fountain on the energy balance and the freezing events was significant. The contribution of heat flux by conduction q_G was minimal as it only varied between -1 to 3 W m⁻² with a mean of 0 W m⁻². The energy contributing to surface temperature changes (q_T) was insignificant in comparison to the energy spent on freezing and melting ($q_{freeze/melt}$). The resulting bulk temperature and the surface temperature are shown in Fig. ?? (b). For the total considered period, $q_{freeze/melt}$ accounted for 30% of overall energy turnover. The energy turnover is calculated as the sum of energy fluxes in absolute values. q_{LW} accounted for 22%, followed by q_S (20%), q_{SW} (16%), q_L (5%), q_F (6%), q_T (1%) and q_G (0%).

Fig. 6 (c) represents the mass fluxes associated with these energy exchanges expressed in m w.e. It shows the ice and meltwater formed due to q_{melt} , snow accumulated due to precipitation, water vapour deposition and sublimation due to q_L .

The total water used for the Icestupa development includes contributions from the fountain (96.7%), snowfall (2.9 %), deposition (0.5 %) as shown in Table ???. Therefore, in the case of CH21 we used a water input of 1,034,328 kg, with a resultant storage efficiency of 19 %.

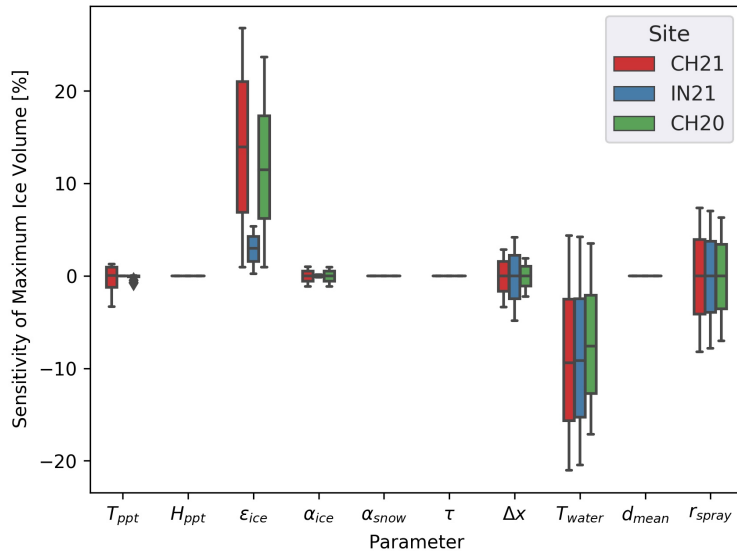


Figure 8. Sensitivities of maximum ice volume to all the uncertain parameters used in the model (Table 2).

5 MODEL SENSITIVITY AND UNCERTAINTY ANALYSIS

284 The icestupa model can be regarded as a function $f(x_1, x_2 \dots, x_n) = (y_1, y_2 \dots, y_m)$, where
 285 ($x_1, x_2 \dots, x_n$) are the model parameters and ($y_1, y_2 \dots, y_m$) are the model outputs. The influence of each
 286 parameter on the output variables of interest were quantified and the most important physical parameters
 287 for the subsequent uncertainty analysis were determined. The sensitivity of a parameter x_j is determined
 288 by keeping all other parameters $x_i, i \neq j$ fixed at their baseline value and varying x_j within values that are
 289 physically plausible.

290 A sensitivity study on the parameters (listed in Table 2) was performed with the maximum ice volume
 291 as the target variable. All the parameters were assumed to be independent of each other with a uniform
 292 distribution. This assumption ignores the auto-correlation present among the parameters associated with
 293 the albedo parameterisation. The range of uncertain parameters were set based on available literature values
 294 or varied $\pm 5\%$ from the base value if no such reference was available. The uncertainty of all the site
 295 parameters were caused due to parallax errors during manual measurement. This was quantified with a
 296 range of $\pm 1\%$ from the base value. However, it must be kept in mind that, even though intended to be as
 297 objective as possible, the selection of a parameter range has a subjective part that influences the results and
 298 conclusions obtained in this analysis. The variation of the model outputs y_k is evaluated to quantify the
 299 local sensitivities $s_{j,k}$ that are defined here as the 95% range of the simulated outputs.

300 To perform the uncertainty analysis, we included only parameters that influence the maximum ice volume
 301 by at least $0.1 m^3$. All other parameters were fixed at their baseline value. Fig. 8 shows all the variance
 302 produced by these uncertain parameters in maximum ice volume calculation.

303 In total, the sensitivity analysis required 120 simulations, and the uncertainty analysis a total of 662
 304 simulations.

Table 3. AIR Results

AIR	IN21	CH21	CH20	CH19
Max Ice Volume [m^3]	703	156	107	1
Storage Efficiency [%]	18	19	14	3
Storage Duration [days]	?	169	93	45
Validation RMSE [m^3]	59	13	25	0.2

6 DISCUSSION

305 **6.1 Important assumptions**

306 In the sensitivity and uncertainty analysis presented above, we did not account for several general
 307 assumptions and parametrisation choices that may cause model errors. Some assumptions and their
 308 potential to cause errors are discussed below.

- 309 • Turbulent Sensible and Latent Heat Fluxes: The method used to calculate the turbulent heat fluxes
 310 by Garratt (1992) assumes that the turbulent heat fluxes are acting over a uniform planar surface to
 311 determine the roughness length. Since our application is on a conical surface, the distance to the ice
 312 surface is not uniform and well defined. Hence, z_{ice} has no real physical significance here.
- 313 • Droplet flight time loss: Water losses during the flight time of fountain droplets were neglected making
 314 all the fountain spray available for freezing. For the CH21 experiment, inclusion of this parameter does
 315 not influence results since it is already accounted for in the runoff water discharge rate which was at
 316 least $3 l min^{-1}$.
- 317 • Nucleation of droplets: Corresponding to droplet flight time, ice/snow formation is also possible before
 318 surface contact if nucleation occurs during flight time. For the CH21 experiment, this process will
 319 further increase the freeze rate and hence the storage efficiency. This process is neglected for model
 320 simplicity.
- 321 • Shape Effects: The suppression of heat exchange between the snow/ice surface and the air adjacent
 322 to the surface effectively slows down snow/ice ablation in spring and promotes the stagnation of the
 323 cold air within topographical depressions (Fujita et al., 2010). The quantitative contribution of the
 324 atmospheric decoupling over melting snow/ice for the total mass and energy balance is ignored in the
 325 model.

7 CONCLUSIONS

326 We outlined a methodology for estimating ice, liquid water, water vapour and runoff quantities produced
 327 during the construction of an AIR using measurements of fountain spray rate, air temperature, radiation,
 328 humidity, pressure, wind and cloudiness at four different study sites. The comparison with all the validation
 329 measurements at two different dates during the experiment led to satisfying results as shown in Table 3.

330 The model results support the hypothesis that there could be considerable water loss during the formation
 331 of AIR particularly due to excessive fountain spray. Further experiments at different locations with different
 332 fountains are required to better understand the influence of construction decisions on the results.

8 APPENDIX

8.1 Ladakh Icestupa 2014/15

A 20 m tall Icestupa (Wangchuk, 2015c) was built in Phyang village, Ladakh at an altitude of 3500 m a.s.l. Assuming a conical shape with a diameter of 20 m, the corresponding volume of this Icestupa becomes 2093 m³ or 1,920 m³ w.e. The fountain sprayed water at a rate of 210 l min⁻¹ (Wangchuk, 2015e) from 21st January (Wangchuk, 2015a) to at least until 5th March 2015 (Wangchuk, 2015b) (around 43 nights). Assuming fountain spray was active for 8 hours each night, we estimate water consumption to be around 4,334 m³. Thus, during the construction/freezing period of the Icestupa, roughly 56 % of the water provided was wasted. The actual water loss is bound to be much higher due to further vapour losses during the melting period. This Icestupa completely melted away on 6th July 2015 (Wangchuk, 2015d). Therefore, the storage duration was 166 days or roughly 5 months.

REFERENCES

- Apel, H., Abdykerimova, Z., Agalhanova, M., Baimaganbetov, A., Gavrilko, N., Gerlitz, L., et al. (2018). Statistical forecast of seasonal discharge in central asia using observational records: development of a generic linear modelling tool for operational water resource management. *Hydrology and Earth System Sciences* 22, 2225–2254. doi:10.5194/hess-22-2225-2018
- Bonales, L. J., Rodriguez, A. C., and Sanz, P. D. (2017). Thermal conductivity of ice prepared under different conditions. *International Journal of Food Properties* 20, 610–619. doi:10.1080/10942912.2017.1306551
- Buytaert, W., Moulds, S., Acosta, L., Bievre, B. D., Olmos, C., Villacis, M., et al. (2017). Glacial melt content of water use in the tropical andes. *Environmental Research Letters* 12, 114014. doi:10.1088/1748-9326/aa926c
- Chen, Y., Li, W., Deng, H., Fang, G., and Li, Z. (2016). Changes in central asia's water tower: Past, present and future. *Nature* doi:10.1088/1748-9326/aa926c
- [Dataset] Copernicus Climate Change Service (C3S) (2017). Era5: Fifth generation of ecmwf atmospheric reanalyses of the global climate. [Available at <https://cds.climate.copernicus.eu/cdsapp#!/home>, accessed 2019-10-01]
- Cuffey, K. M. and Paterson, W. S. B. (2010). *The Physics Of Glaciers* (Elsevier)
- Fujita, K. and Ageta, Y. (2000). Effect of summer accumulation on glacier mass balance on the tibetan plateau revealed by mass-balance model. *Journal of Glaciology* 46, 244–252. doi:10.3189/172756500781832945
- Fujita, K., Hiyama, K., Iida, H., and Ageta, Y. (2010). Self-regulated fluctuations in the ablation of a snow patch over four decades. *Water Resources Research* 46, W11541. doi:10.1029/2009WR008383
- Garratt, J. R. (1992). *The Atmospheric Boundary Layer* (Cambridge University Press)
- Grossman, D. (2015). As himalayan glaciers melt, two towns face the fallout [Available at https://e360.yale.edu/features/as_himalayan_glaciers_melt_two_towns_face_the_fallout, accessed 2019-10-01]
- Hock, R. (2005). Glacier melt: a review of processes and their modelling. *Progress in Physical Geography: Earth and Environment* 29, 362–391
- Hock, R., Rasul, G., Adler, C., Cáceres, B., Gruber, S., Hirabayashi, Y., et al. (2019). 2019: High mountain areas. *IPCC Special Report on the Ocean and Cryosphere in a Changing Climate* [H.-O. Pörtner, D.C. Roberts, V. Masson-Delmotte, P. Zhai, M. Tignor, E. Poloczanska, K. Mintenbeck, A. Alegría, M. Nicolai, A. Okem, J. Petzold, B. Rama, N.M. Weyer (eds.)]

- 374 Hoelzle, M., Barandun, M., Bolch, T., Fidde, J., Gafurov, A., Muccione, V., et al. (2019). *The status and*
375 *role of the alpine cryosphere in Central Asia*. doi:10.4324/9780429436475-8
- 376 Hori, M., Aoki, T., Tanikawa, T., Motoyoshi, H., Hachikubo, A., Sugiura, K., et al. (2006). In-situ
377 measured spectral directional emissivity of snow and ice in the 8–14 micrometer atmospheric window.
378 *Remote Sensing of Environment* 100, 486 – 502
- 379 Immerzeel, W. W., Lutz, A. F., Andrade, M., Bahl, A., Biemans, H., Bolch, T., et al. (2019). Importance
380 and vulnerability of the world's water towers. *Nature* 577, 364 – 369. doi:10.1038/s41586-019-1822-y
- 381 Meteoblue (2020). Climate schwarzsee [Available at https://www.meteoblue.com/en/weather/historyclimate/climatemodeled/schwarzsee_switzerland_11790334, accessed 2019-10-01]
- 382 Mölg, T. and Hardy, D. R. (2004). Ablation and associated energy balance of a horizontal glacier surface
383 on kilimanjaro. *J. Geophys. Res.-Atmos.* 109, 1–13. doi:10.1029/2003JD004338
- 384 Nüsser, M., Dame, J., Kraus, B., Baghel, R., and Schmidt, S. (2019a). Socio-hydrology of artificial glaciers
385 in ladakh, india: assessing adaptive strategies in a changing cryosphere. *Regional Environmental Change*
386 doi:10.1007/s10113-018-1372-0
- 387 Nüsser, M., Dame, J., Parveen, S., Kraus, B., Baghel, R., and Schmidt, S. (2019b). Cryosphere-Fed
388 Irrigation Networks in the Northwestern Himalaya: Precarious Livelihoods and Adaptation Strategies
389 Under the Impact of Climate Change. *Mountain Research and Development* 39. doi:10.1659/
390 MRD-JOURNAL-D-18-00072.1
- 391 Oerlemans, J. and Knap, W. H. (1998). A 1 year record of global radiation and albedo in the
392 ablation zone of morteratschgletscher, switzerland. *Journal of Glaciology* 44, 231–238. doi:10.
393 3189/S0022143000002574
- 394 Scherrer, S. C. (2020). Temperature monitoring in mountain regions using reanalyses: lessons from the
395 alps. *Environmental Research Letters* 15, 044005
- 396 Schmidt, L. S., Aðalgeirsdóttir, G., Guðmundsson, S., Langen, P. L., Pálsson, F., Mottram, R., et al. (2017).
397 The importance of accurate glacier albedo for estimates of surface mass balance on vatnajökull: evaluating
398 the surface energy budget in a regional climate model with automatic weather station observations. *The
399 Cryosphere* 11, 1665–1684. doi:10.5194/tc-11-1665-2017
- 400 Unger-Shayesteh, K., Vorogushyn, S., Farinotti, D., Gafurov, A., Duethmann, D., Mandychev, A., et al.
401 (2013). What do we know about past changes in the water cycle of central asian headwaters? a review.
402 *Global and Planetary Change* 110, 4 – 25. doi:10.1016/j.gloplacha.2013.02.004. Water in Central Asia
403 – Perspectives under global change
- 404 Wangchuk, S. (2014). Ice stupa artificial glaciers of ladakh [Available at www.indiegogo.com/projects/ice-stupa-artificial-glaciers-of-ladakh#, accessed 2019-10-01]
- 405 Wangchuk, S. (2015a). The good news at ice stupa 24th january 2015 [Available at <http://icestupa.org/news/the-good-news-at-ice-stupa>, accessed 2019-10-01]
- 406 Wangchuk, S. (2015b). Ice stupa artificial glacier inaugurated
407 5th of march 2015 [Available at <http://icestupa.org/news/ice-stupa-artificial-glacier-inaugurated-5th-of-march>, accessed
408 2019-10-01]
- 409 Wangchuk, S. (2015c). Ice stupa surpasses guiness world record [Available at <http://icestupa.org/news/ice-stupa-surpasses-guinness-world-record>, accessed 2019-10-01]
- 410 Wangchuk, S. (2015d). Ice stupa way of celebrating a special day [Available at <http://icestupa.org/news/ice-stupa-way-of-celebrating-a-special-day6th-of-ju>, accessed
411 2019-10-01]

- 419 Wangchuk, S. (2015e). World water day at ice stupa [Available at <http://icestupa.org/news/world-water-day-at-ice-stupa>, accessed 2019-10-01]
- 420
- 421 WMO (2018). *Guide to Instruments and Methods of Observation* (World Meteorological Organization ;
- 422 2018 (2018 Edition))
- 423 Woolf, H. M. (1968). *On the Computation of Solar Elevation Angles and the determination of sunrise and*
- 424 *sunset times* (National Aeronautics and Space Administration)
- 425 Zhou, S., Kang, S., Gao, T., and Zhang, G. (2010). Response of zhadang glacier runoff in nam co basin,
- 426 tibet, to changes in air temperature and precipitation form. *Chinese Science Bulletin* 55, 2103–2110.
- 427 doi:10.1007/s11434-010-3290-5